JOURNAL OF SPACECRAFT AND ROCKETS
Vol. 43, No. 1, January–February 2006

Simulation of Hypervelocity Impact Effects on Reinforced Carbon–Carbon

Young-Keun Park* and Eric P. Fahrenthold†
University of Texas at Austin, Austin, Texas 78712

Spacecraft operating in low Earth orbit face a significant orbital debris impact hazard. Of particular concern, in the case of the space shuttle, are impacts on critical components of the thermal protection system. Recent research has formulated a new material model of reinforced carbon–carbon, for use in the analysis of hypervelocity impact effects on the space shuttle wing leading edge. The material model has been validated in simulations of published impact experiments and applied to model orbital debris impacts at velocities beyond the range of current experimental methods. The results suggest that momentum scaling, which has been used to correlate the available experimental database, can predict the size of wing leading-edge perforations at impact velocities as high as 13 km/s.

Nomenclature

D = projectile diameter
$\boldsymbol{D}$ = rate of deformation tensor
D_c = coating spall diameter
D_p = perforation diameter
d = shear damage variable
$\boldsymbol{E}^e$ = elastic strain tensor
$\boldsymbol{E}^p$ = plastic strain tensor
$\bar{\boldsymbol{E}}$ = deviatoric strain tensor
$\boldsymbol{e}$ = Euler parameter vector
$\boldsymbol{F}$ = deformation gradient tensor
$\boldsymbol{L}$ = velocity gradient tensor
N_e = number of elements
$\boldsymbol{R}$ = rotation matrix
$\boldsymbol{S}$ = deviatoric stress tensor
$\boldsymbol{S}^p$ = effective stress tensor
s = entropy density
v = impact velocity
δ_{ij} = Kronecker delta
ε^p = effective plastic strain
$\dot{\varepsilon}$ = deviatoric strain rate
θ = temperature
ρ = density
ϕ = impact obliquity
ψ = strain energy density

Introduction

CARBON–CARBON composites offer an unusual combination of thermal and mechanical properties.[1] Their light weight and high-temperature strength satisfy some very stringent design requirements for reusable orbital vehicles.[2] The wing leading edge of the space shuttle, subject to severe thermal reentry loads, is constructed of reinforced carbon–carbon (RCC) panels, coated in silicon carbide to prevent oxidation.[3] Although the thermal properties of RCC composites are well understood,[4] much less is known about their dynamic mechanical properties. The loss of the Space Shuttle *Columbia*,[5] apparently because of impact damage on the wing leading edge, has motivated recent experimental[6] and computational[7] work aimed at developing a better understanding of the impact response of thermal protection materials.

The wing leading-edge damage to *Columbia* was unexpected, the result of a relatively low-velocity impact by a relatively low-density projectile.[8] Another impact damage hazard, caused by space debris in low Earth orbit, has long been recognized. This threat involves projectiles of very low mass, but much higher density, and impact velocities as high as 15 km/s. The debris shielding on the International Space Station is designed, in selected areas, to defeat centimeter-sized aluminum projectiles. Although the likelihood of such a projectile striking the space shuttle is quite low, orbital debris damage by much smaller projectiles is routinely observed during postmission inspections of the vehicle. Previous experimental research has investigated the response of space shuttle thermal protection materials to orbital debris impact. The latter work demonstrated that a 0.628-cm-diam spherical aluminum projectile can produce a 2.9-cm-diam perforation in the space shuttle wing leading edge, at impact velocity (7 km/s) typical of low-Earth-orbit debris.[9]

Because of the high cost of carbon–carbon composites and the long fabrication lead times associated with the preparation of test samples, impact testing of RCC materials has been limited. In addition, the limitations of current experimental technology preclude hypervelocity impact testing over the entire projectile mass and kinetic energy range of interest. As a result, numerical simulation can serve as an important complement to experimental studies of the impact response of RCC materials. Numerical models validated by comparison with experiment at velocities below 8 km/s can be used to extrapolate results into a higher-velocity impact regime. A coordinated experimental and computational approach to the study of RCC response to insulating foam impacts has proven to be productive[10]; the present paper extends the latter computational work to projectiles and impact velocities associated with orbital debris impact. In particular it develops a new anisotropic, rate-dependent material model for reinforced carbon–carbon, validates that model in three-dimensional simulations of published hypervelocity impact experiments, and applies the validated formulation in simulations of impacts at velocities beyond the experimental range. The results indicate that momentum scaling, which correlates the available experimental impact data,[9] can be used to predict the diameters of RCC perforations for hypervelocity projectiles at velocities as high as 13 km/s.

The present paper is organized as follows. The first section outlines the hybrid particle finite element method used in the present study, including the imbedded large deformation kinematics and general functional forms for the associated constitutive relations. The second section discusses published experimental results on the properties of RCC. The third section develops an RCC constitutive model, formulated for use in hypervelocity impact applications and reflecting important mechanical characteristics described in the

---

Received 26 October 2004; revision received 4 May 2005; accepted for publication 4 May 2005.

*Graduate Research Assistant, Department of Mechanical Engineering, 1 University Station C2200.

†Professor, Department of Mechanical Engineering, 1 University Station C2200. Member AIAA.

material testing literature. The fourth section validates and applies the developed model in a series of three-dimensional impact simulations. The last section presents conclusions, based on the results of the current numerical study.

Numerical Method

The material model described in this paper was developed for application in a specific numerical framework, the hybrid particle finite element formulation of Refs. 11 and 12. To provide appropriate context, this section summarizes the latter numerical formulation, details certain element level kinematics, and provides functional forms for the required constitutive relations. The kinematic and constitutive modeling framework assumed here has wide scope, so that the material model described in the present paper can be adapted for use in shock physics codes, which are based on alternative numerical modeling schemes.[13]

The hybrid particle finite element model employed here takes an explicit state-space form. The state equations consist of evolution equations for the following variables: 1) translational and rotational momentum vectors for the three-dimensional motion of ellipsoidal particles; 2) center-of-mass position vectors and Euler parameters for the particles, the latter providing a singularity free description of particle rotations; 3) density and internal energy for each particle; and 4) damage and plastic internal state variables for each finite element. The state equations are derived using a thermomechanical formulation of the Lagrange equations. All inertia effects are modeled using the particles, whose mass centers are also nodal coordinates for the finite elements. The volumetric thermomechanical response of the modeled medium, in compressed states, is described by an equation of state for the particles, which can take either an analytic or tabular form.

The material modeling work described in the present paper develops two specific components of the general numerical formulation: 1) a strain energy density in shear, one part of the thermomechanical Lagrangian for the modeled particle-element system; and 2) a plasticity model, which specifies evolution equations for the plastic internal state variables, equations that serve as nonholonomic constraints on the system level model. The strain energy density in shear takes the general functional form

$$\psi = \psi(d, \boldsymbol{e}, \bar{\boldsymbol{E}}, \boldsymbol{E}^p) \tag{1}$$

where $\boldsymbol{e}$ is a vector of Euler parameters, which relates a material reference frame for each element to a single global Cartesian reference frame. The evolution equations for the plastic strain components take the general functional form

$$\dot{\boldsymbol{E}}^p = \dot{\boldsymbol{E}}^p(\rho, s, d, \varepsilon^p, \dot{\varepsilon}, J, \boldsymbol{e}, \bar{\boldsymbol{E}}, \boldsymbol{E}^p) \tag{2}$$

where

$$J = \det(\boldsymbol{F}) \tag{3}$$

The strain and strain-rate variables that appear in the preceding functional forms are defined by the following large deformation kinematics.[14] The deviatoric strain is

$$\bar{\boldsymbol{E}} = \tfrac{1}{2}(\bar{\boldsymbol{C}} - \boldsymbol{I}) \tag{4}$$

where

$$\bar{\boldsymbol{C}} = \bar{\boldsymbol{F}}^T \bar{\boldsymbol{F}}, \qquad \bar{\boldsymbol{F}} = (\det \boldsymbol{F})^{-\frac{1}{3}} \boldsymbol{F} \tag{5}$$

The elastic shear strain is defined as

$$\boldsymbol{E}^e = \bar{\boldsymbol{E}} - \boldsymbol{E}^p \tag{6}$$

where the flow rule for the plastic stain tensor must satisfy the isochoric plastic deformation constraint

$$\mathrm{tr}(\boldsymbol{C}^{p\,-T} \dot{\boldsymbol{C}}^p) = 0, \qquad \boldsymbol{C}^p = \boldsymbol{I} + 2\boldsymbol{E}^p \tag{7}$$

The effective plastic strain is determined by integrating the rate relation

$$\dot{\varepsilon}^p = \|\dot{\boldsymbol{E}}^p\| \tag{8}$$

with the indicated invariant operator defined by

$$\|\boldsymbol{T}\| = \left[\tfrac{1}{2}\mathrm{tr}(\boldsymbol{T}^T\boldsymbol{T})\right]^{\frac{1}{2}} \tag{9}$$

for any second-order tensor $\boldsymbol{T}$. The deviatoric strain rate is

$$\dot{\varepsilon} = \|\boldsymbol{D}'\|, \qquad \boldsymbol{D}' = \boldsymbol{D} - \tfrac{1}{3}\mathrm{tr}(\boldsymbol{D})\boldsymbol{I} \tag{10}$$

$$\boldsymbol{D} = \tfrac{1}{2}(\boldsymbol{L} + \boldsymbol{L}^T), \qquad \boldsymbol{L} = \dot{\boldsymbol{F}}\boldsymbol{F}^{-1} \tag{11}$$

In the case of anisotropic materials, the constitutive response is described in a material reference frame. Here an Euler parameter vector

$$\boldsymbol{e} = [e_0 \quad e_1 \quad e_2 \quad e_3]^T, \qquad \boldsymbol{e}^T\boldsymbol{e} = 1 \tag{12}$$

is used to define a rotation matrix ($\boldsymbol{R}$) for each element

$$\boldsymbol{R} = \boldsymbol{A}\boldsymbol{G}^T \tag{13}$$

$$\boldsymbol{A} = \begin{bmatrix} -e_1 & e_0 & -e_3 & e_2 \\ -e_2 & e_3 & e_0 & -e_1 \\ -e_3 & -e_2 & e_1 & e_0 \end{bmatrix} \tag{14}$$

$$\boldsymbol{G} = \begin{bmatrix} -e_1 & e_0 & e_3 & -e_2 \\ -e_2 & -e_3 & e_0 & e_1 \\ -e_3 & e_2 & -e_1 & e_0 \end{bmatrix} \tag{15}$$

which relates a material reference frame in each element to the global Cartesian system used in the numerical simulations. The rotation matrix relates vector components $\boldsymbol{p}$ in the global coordinate system to corresponding components $\boldsymbol{q}$ described in the material reference frame, using

$$\boldsymbol{p} = \boldsymbol{R}\boldsymbol{q} \tag{16}$$

The corresponding transformation relation for second-order tensor components is

$$\boldsymbol{P} = \boldsymbol{R}\boldsymbol{Q}\boldsymbol{R}^T \tag{17}$$

where the components $\boldsymbol{P}$ refer to the global frame and the components $\boldsymbol{Q}$ refer to the material reference frame.

Reinforced Carbon–Carbon

The published material property database for carbon–carbon composites is limited by material costs and proprietary considerations. On the other hand, the complex nature of both the material and the application of interest here means that a rather wide range of experiments are needed to fully characterize its constitutive response. This section discusses some properties of RCC of particular significance in hypervelocity impact applications.

The most directly relevant experimental results are those of Lu et al.,[6] who performed tests at Sandia National Laboratories on samples taken from space shuttle wing leading-edge panels, in support of the *Columbia* accident investigation. They provide data on elastic moduli as well as strength measurements obtained from tension, bending, and compression tests. Although the elastic moduli measured in tension and compression were similar, strength in compression was approximately double that in tension. In addition they reported a strain-rate dependence of the tensile strength, observing a 15% increase in strength as the loading rate increased from 1 to 200 s^{-1}. Finally they noted that removal of the silicon-carbide coating from the tested samples showed little effect on the measured mechanical properties.

Several different authors have reported results of shear tests performed on carbon–carbon composites.[15–20] In the case of the RCC, interlaminar shear strength and stiffness are of interest because oblique hypervelocity impacts will in general lead to multiaxial loading. The published shear test data show that interlaminar shear stiffness and strength can differ by factors of approximately two and four respectively, from their in-plane counterparts.

Perhaps the most unusual property of RCC is its increase in strength with temperature,[17,21] by as much as a factor of two, as compared to the thermal softening response observed in metals. The high-temperature strength of RCC is important in hypervelocity impact applications, due to the adiabatic heating typically associated with shock loading.

The preceding references, along with the equation of state literature[22] and published data on the thermal properties of RCC,[4,23] were used to estimate material parameters for the simulations reported in a later section. Although additional tests on space shuttle wing leading-edge panels, like those reported by Lu et al., are needed, the cited references represent the best data available to the authors at the time the simulations were conducted.

Material Model

Composite materials are used in structural,[24] orbital debris shielding,[25] and thermal protection[4] applications on a variety of spacecraft; hence, their response to hypervelocity impact effects has been analyzed in a number of previous experimental[26] and computational[27] studies. Previous material modeling work has considered both micromechanical[28] and anisotropic continuum models.[28] The present paper employs an anisotropic continuum approach because the high computational cost of micromechanical models normally precludes their use in structural scale simulations. Large deformation, anisotropic continuum models of composite materials[29] normally address shock physics problems[30] by extending small strain formulations originally developed for applications in structural mechanics.[31] In an alternative approach, the present work starts with the finite-strain, hybrid particle element kinematics discussed in an earlier section and then formulates 1) an anisotropic strain energy density function, which depends on a general deviatoric Lagrangian strain tensor, and 2) an anisotropic, temperature, and rate-dependent plastic flow rule that depends on an effective stress[32] and satisfies a general isochoric deformation constraint. Both the strain energy density function and the plastic flow rule, 1) account for differences in material response under tension and compression, 2) account for material reference frame dependence under large deformations, and 3) satisfy first and second law thermodynamic constraints. The approach used here has been applied with success to model isotropic materials.[33] It is motivated by a focus on hypervelocity problems, where large deformation dynamics are of central interest, and by the kinematic form of the hybrid numerical method used in the present paper. As indicated in the later section on simulations, this material modeling approach provides an accurate description of hypervelocity impact effects in reinforced carbon–carbon. Potential application of the formulation to model impact in other composites, such as graphite-epoxy or Kevlar-epoxy, is of interest for future work.

In the case of an orthotropic material, with distinct elastic moduli in tension and compression, the shear strain energy density per unit reference volume is

$$\psi = (1-d)\mu_o \frac{1}{2}\sum_{i=1}^{3} \mu_{ii}\left[(1+\gamma_i) + (1-\gamma_i)\,\mathrm{sgn}\left(E_{ii}^{em}\right)\right]\left(E_{ii}^{em}\right)^2 + (1-d)\mu_o \sum_{i=1}^{3}\sum_{j=1}^{3}(1-\delta_{ij})\mu_{ij}\left(E_{ij}^{em}\right)^2 \tag{18}$$

where μ_o is a reference elastic modulus and the parameters $\mu_{ij} = \mu_{ji}$ are dimensionless constants. The parameters γ_i are the ratios of the elastic moduli in compression to those in tension, and the E_{ij}^{em} are the components of the elastic shearing strain, expressed in a material reference frame. Note that this function is continuous because a change in modulus from tension to compression occurs when the corresponding material strain component is zero.

A plastic flow rule for an anisotropic, rate-dependent material, which satisfies the aforementioned isochoric plastic deformation constraint, can be obtained by extending a large-strain Lagrangian formulation previously developed for use in hypervelocity impact applications.[34] The flow rule is

$$\dot{\boldsymbol{E}}^p = (\dot{\lambda}/\|\boldsymbol{S}^p\|)\underline{\underline{\boldsymbol{N}}}^p\underline{\underline{\boldsymbol{N}}}\,\underline{\underline{\boldsymbol{M}}}\,\underline{\underline{\boldsymbol{M}}}^p\,\boldsymbol{S}^p \tag{19}$$

where $\dot{\lambda}$ is a positive proportionality coefficient,

$$\boldsymbol{S}^p = \underline{\underline{\boldsymbol{M}}}^{pT}\underline{\underline{\boldsymbol{M}}}^T\underline{\underline{\boldsymbol{N}}}^T\underline{\underline{\boldsymbol{N}}}^{pT}\boldsymbol{S} \tag{20}$$

$$\boldsymbol{S} = \frac{\partial\psi}{\partial\boldsymbol{E}^e} \tag{21}$$

The first two coefficients in the flow rule impose the isochoric plastic deformation constraint and are defined by

$$\underline{\underline{\boldsymbol{N}}}^p\boldsymbol{T} = (1/2\|\boldsymbol{C}^p\|)(\boldsymbol{C}^p\boldsymbol{T} + \boldsymbol{T}\boldsymbol{C}^p) \tag{22}$$

$$\underline{\underline{\boldsymbol{N}}}\boldsymbol{T} = \boldsymbol{T} - \tfrac{1}{3}\mathrm{tr}(\boldsymbol{T})\boldsymbol{I} \tag{23}$$

for any symmetric second-order tensor $\boldsymbol{T}$. The third coefficient performs a component transformation from a material reference frame to a fixed global frame and is defined by

$$\underline{\underline{\boldsymbol{M}}}^T\boldsymbol{T} = \boldsymbol{R}^T\boldsymbol{T}\boldsymbol{R} \tag{24}$$

for any symmetric second-order tensor $\boldsymbol{T}$. The last coefficient in the flow rule defines an effective stress transformation, in a material reference frame, using

$$\underline{\underline{\boldsymbol{M}}}^{pT}\boldsymbol{P} = \boldsymbol{Q} \tag{25}$$

for symmetric second-order tensors $\boldsymbol{P}$ and $\boldsymbol{Q}$, with component forms

$$Q_{ii} = \frac{2\alpha_{ii}P_{ii}}{(1+\beta_{ii}) + (1-\beta_{ii})\,\mathrm{sgn}\left(E_{ii}^{em}\right)} \qquad i = 1, 2, 3 \tag{26}$$

$$Q_{ij} = \frac{2\alpha_{ij}P_{ij}}{(1+\beta_{ij}) + (1-\beta_{ij})\,\mathrm{sgn}(J-1)} \qquad i \neq j \tag{27}$$

The parameter $\alpha_{ij} = \alpha_{ji}$ is the ratio of a reference yield stress to the yield stress for the ijth stress component, while the parameter $\beta_{ij} = \beta_{ji}$ is the ratio of the strength in compression to that in tension for the ijth stress component.

The rate-dependent, strain-hardening, thermal-softening yield function is

$$f = \|\boldsymbol{S}^p\| - Y \tag{28}$$

where Y is the yield stress

$$Y = \tfrac{1}{2}(1-d)Y_o(1-\kappa\theta^H)(1+\eta\varepsilon^p)^n[1+\zeta\,\log(\dot{\varepsilon}/\dot{\varepsilon}_o)]^m \tag{29}$$

with Y_o the reference yield stress, η a strain-hardening coefficient, n a strain-hardening exponent, ζ a strain-rate-hardening coefficient, m a strain-rate-hardening exponent, $\dot{\varepsilon}_o$ a reference strain rate, κ a thermal-softening coefficient, and θ^H the homologous temperature

$$\theta^H = (\theta - \theta_o)/(\theta_m - \theta_o) \tag{30}$$

where θ_o and θ_m are reference and melt temperatures.

In a numerical implementation, the aforementioned plastic flow rule is expressed in incremental form. That is the incremental plastic strain at each time step is computed using the incremental proportionality coefficient

$$\Delta\lambda = \max\left[0, \frac{\|\boldsymbol{S}^p\| - Y}{(1-d)2\mu_o}\right] \tag{31}$$

The shear damage variable d models the transition from an intact to a failed medium, evolving from an initial value of zero to a final value of one over a fixed number of time steps[35] when any stipulated element failure criterion is satisfied. The simulations discussed in the next section incorporate accumulated plastic strain, melt temperature, and maximum compression failure criteria, although other criteria can be accommodated.

Impact Simulations

The material model just described was applied in a series of three-dimensional simulations of hypervelocity impacts on reinforced carbon–carbon. The simulations employed a hybrid particle finite element method and the material properties listed in Tables 1 and 2. An initial set of simulations was used to validate the material model, compare results obtained using analytic (Mie Gruneisen) and tabular[36] (SESAME 3715) equations of state for the projectile, and check numerical convergence of the simulation results. A second series of simulations was then performed to estimate orbital debris impact effects at velocities beyond the range of current experimental methods. Note that tabular equation of state data were not available for the target materials.

Table 1 Material properties

Material property	Aluminum	Silicon carbide	Carbon–carbon
Reference bulk modulus, Mbar	0.784	2.21	0.0576
Reference shear modulus, Mbar	0.271	0.240	0.0718
Reference sound speed, cm μs^{-1}	0.539	0.829	0.191
Mie–Gruneisen gamma	1.97	0.95	0.24
Mie–Gruneisen slope	1.34	1.21	1.33
Reference density, $g \cdot cm^{-3}$	2.70	3.21	1.58
Reference yield stress, kbar	2.90	0.771	0.771
Specific heat, $bar \cdot cm^3\ g^{-1} K^{-1}$	8.84	7.12	7.12
Strain-hardening coefficient	125	10	2
Strain-hardening exponent	0.1	1.0	1.0
Strain-rate-hardening coefficient	0.0	0.0	0.1
Strain-rate-hardening exponent	0.0	0.0	1.0
Reference strain rate, s^{-1}	0	0	0.01
Thermal-softening coefficient	0.567	0.0	−1.0
Melt temperature, K	1,220	3,840	3,840
Maximum compression	100	100	100
Plastic failure strain	1.00	0.10	0.50

Table 2 Material model parameters

Parameter	Silicon carbide	Carbon–carbon
$\gamma_1 = \gamma_2 = \gamma_3$	10.0	1.00
$\mu_{11} = \mu_{22} = \mu_{33}$	0.10	1.00
$\mu_{12} = \mu_{23}$	1.00	0.50
μ_{13}	1.00	1.00
$\alpha_{11} = \alpha_{22} = \alpha_{33} = \alpha_{13}$	1.00	1.00
$\alpha_{12} = \alpha_{23}$	1.00	3.73
$\beta_{11} = \beta_{22} = \beta_{33}$	2.00	2.00
$\beta_{12} = \beta_{13} = \beta_{23}$	2.00	2.00

The numerical work presented here is focused on a potential vehicle failure mode studied by NASA in previous experimental research.[9,37] That research considered perforation of the wing leading edge by orbital debris impact, followed by oxidation of exposed carbon–carbon material and excessive heating of the wing structure during reentry. Analytical study of this failure mode involves predicting the size of RCC perforations, as a function of projectile mass and impact velocity. Alternative wing leading-edge panel failure mechanisms, such as excessive delamination under impact loads,[9] are not considered in the present work. However, the large-strain Lagrangian kinematics used here are in general well suited for the analysis of alternative failure modes, which show a strong material history dependence.

The first set of eight simulations modeled NASA Johnson Space Center (JSC) experiments B1028 and B1040,[9] which involved oblique impacts of aluminum spheres on reinforced carbon–carbon target plates at a velocity of 7 km/s. The target plates were 0.63 cm in thickness, including upper- and lower-surface coatings composed of silicon carbide, each 0.08 cm in thickness. Table 3 compares the simulation results, at various model resolutions, to the corresponding experiments. The test data include projectile diameter D, impact velocity v, impact obliquity (ϕ, with 0 deg a normal impact), measured average diameter of the carbon–carbon perforation D_p, and measured average diameter of the target region over which the silicon-carbide coating was removed D_c. The simulation data include number of elements spanning the target thickness N_e, equation of state used to model the aluminum projectile, and simulation results for the average diameter of the carbon–carbon perforation and the average diameter of the target region over which the silicon-carbide coating was removed. The error columns in Table 3 show the percent error in the simulation results, as compared to the corresponding experiments, for the average diameter of the carbon–carbon perforation and the average diameter of the target region over which the silicon-carbide coating was removed. In the high-resolution simulations, the difference in coating spall diameter for the upper and lower plate surfaces was negligible. The corresponding experiments produced coating spall regions with rather irregular shapes, but with average diameters for the upper- and lower-surface regions differing by less than ten percent. Figures 1–4 show example plots for a simulation of experiment B1028. Figure 1 shows the initial configuration, whereas Figs. 2–4 show the simulation results at 50 μs after impact. The sectioned plot in Fig. 4 depicts plate perforation and coating spall similar to that observed in the corresponding experiment. The results of the validation simulations suggest the following conclusions:

1) The material model developed here can provide good estimates of both the RCC perforation diameter and the extent of the spalled coating region, for oblique impacts at seven kilometers per second.

2) Accurate estimates of the RCC perforation diameter require a mesh resolution sufficient to place eight elements across the target plate.

3) Accurate estimates of the diameter of the spalled coating region require a mesh resolution sufficient to place 16 elements across the target plate.

Table 3 Comparison of test and simulation results for NASA JSC experiments B1028 and B1040

Test/simulation number	D, cm	v, km/s	ϕ, deg	N_e	Equation of state	D_p, cm	Error, %	D_c, cm	Error, %
Test B1028	0.628	7.01	45	——	——	2.90	——	4.40	——
Sim B1028a	0.628	7.01	45	8	Mie–Gruneisen	2.60	10.3	3.74	15.0
Sim B1028b	0.628	7.01	45	8	SESAME 3715	2.65	8.6	3.60	18.2
Sim B1028c	0.628	7.01	45	16	Mie–Gruneisen	2.66	8.3	4.05	8.0
Sim B1028d	0.628	7.01	45	24	Mie–Gruneisen	2.67	7.9	4.08	7.3
Test B1040	0.477	6.96	30	——	——	2.20	——	3.75	——
Sim B1040a	0.477	6.96	30	8	Mie–Gruneisen	2.12	3.6	2.95	21.3
Sim B1040b	0.477	6.96	30	8	SESAME 3715	1.97	10.5	2.95	21.3
Sim B1040c	0.477	6.96	30	16	Mie–Gruneisen	2.00	9.1	3.38	9.9
Sim B1040d	0.477	6.96	30	24	Mie–Gruneisen	2.10	4.5	3.48	7.2

Table 4 Computer resource requirements, simulations of NASA JSC experiments

Simulation number	N_e	Total particles (million)	Total elements (million)	Number of processors	Wall clock hours
B1028a	8	0.078	0.036	16	14
B1028c	16	0.572	0.275	64	65
B1028d	24	1.857	0.905	64	340
B1040a	8	0.078	0.036	32	5
B1040c	16	0.572	0.275	64	74
B1040d	24	1.856	0.905	64	347

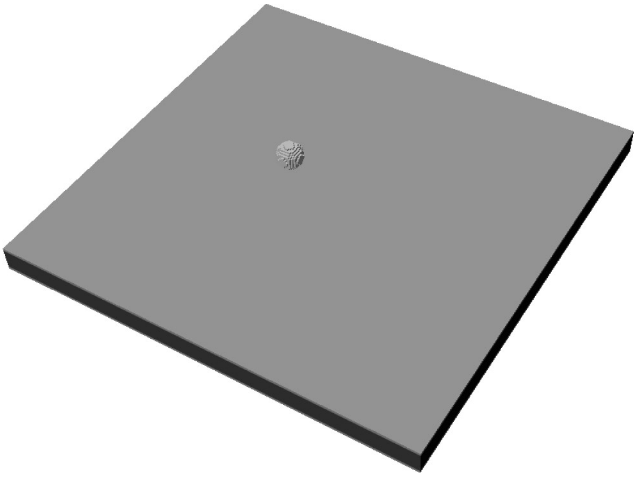

Fig. 1 Initial configuration, simulation of NASA JSC experiment B1028.

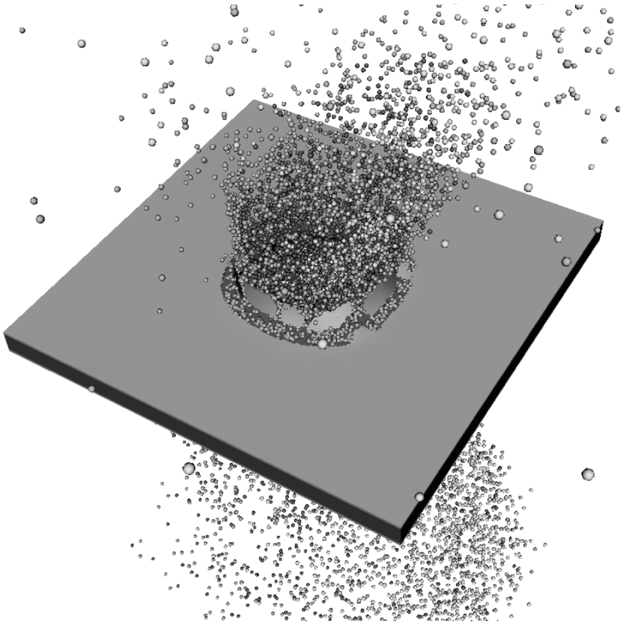

Fig. 2 Particle-element plot of the simulation results at 50 μs after impact.

4) The simulation results are not sensitive to the choice of projectile equation of state. Table 4 shows the relative computational cost of simulations of experiments B1028 and B1040 run at three different mesh densities. As is well known, in three-dimensional models the particle count increases with the cube of the increase in resolution, while the time step decreases linearly with the increase in resolution, so that the total computational cost of high resolution models is considerable.

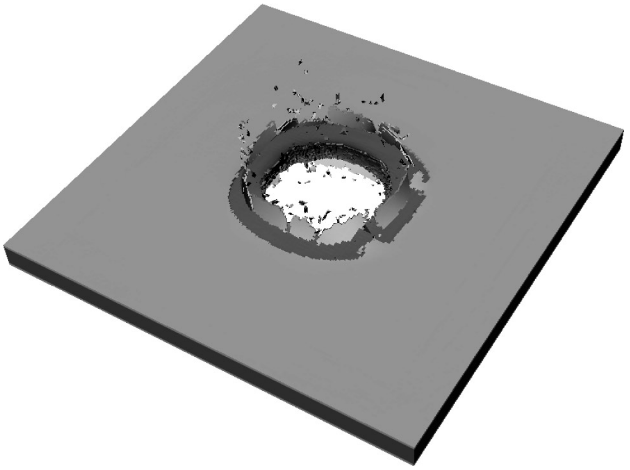

Fig. 3 Element plot of the simulation results at 50 μs after impact.

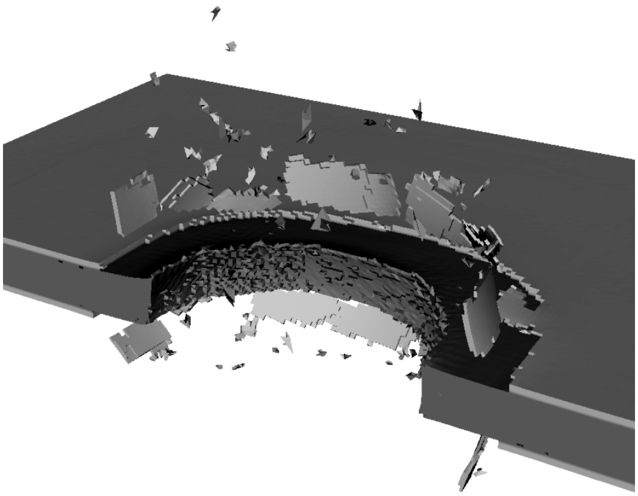

Fig. 4 Sectioned element plot of the simulation results at 50 μs after impact.

A second set of 12 simulations was performed to investigate orbital debris impact effects at velocities beyond the current experimental range. The simulations involved spherical aluminum projectiles, at three different projectile diameters, an impact obliquity of 30 deg and impact velocities of 7, 10, and 13 km/s. In the case of the largest projectile, simulations were performed using both an analytic and a tabular equation of state. The target assumed in these simulations was identical to that involved in the aforementioned experiments. In the target mesh eight elements spanned the plate thickness, so that the resolution level was sufficient to estimate the diameter of the RCC perforations, but not the extent of the region of coating spall. Figure 5 shows simulation results for the diameters of the RCC perforations, as a function of projectile diameter, impact velocity, and projectile equation of state. In Fig. 5, MG denotes the Mie Gruneisen analytic equation of state, and SES denotes the SESAME tabular equation of state. The results of these simulations suggest the following conclusions, for the impact velocity range and impact obliquity considered:

1) Perforation diameters increase with both projectile size and impact velocity, over the full range of the simulations.

2) For a fixed projectile size, perforation diameters increase with impact velocity at an approximately linear rate.

3) For a fixed impact velocity, perforation diameters increase with projectile size, but at a declining rate.

4) The simulation results are not sensitive to the choice of projectile equation of state. Note that Fig. 5 is not a ballistic limit plot; rather, it plots perforation diameter vs impact velocity, so that the indicated trends are not unexpected.

Although the preceding results are informative, they consider a limited range of impact conditions. Hence the scaling of the

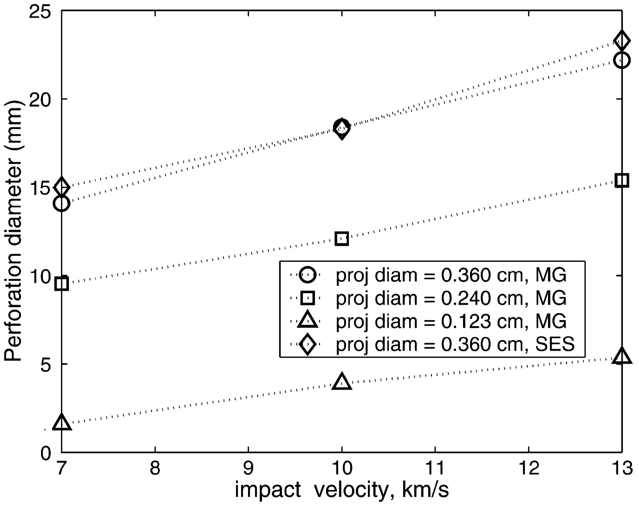

Fig. 5 Simulation results for perforation diameter (obliquity = 30 deg) vs impact velocity.

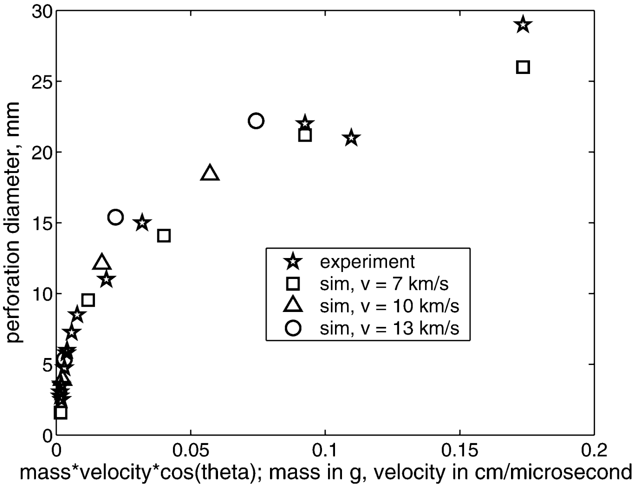

Fig. 6 Perforation diameter vs normal impact momentum, for hypervelocity impact in reinforced carbon–carbon.

simulation results, as compared to the available experimental data, is of considerable interest. Christiansen and Friesen[9] correlated experimental data on hypervelocity perforation of RCC by plotting hole diameter vs the cube root of normal impact momentum, for impact velocities below 8 km/s. Figure 6 shows a plot of perforation diameter vs normal impact momentum for the 11 different projectile size and impact velocity combinations modeled in the present computational study, as well as corresponding data for 15 published experiments.[9,38] The experiments involved projectile diameters ranging from 0.039 to 0.628 cm, impact velocities ranging from 2.49 to 7.32 km/s, and impact obliquities ranging from 0 to 80 deg. The simulations involved a more limited range of projectile diameters (0.123–0.360 cm) and obliquities (30–45 deg), but a much higher range of impact velocities (7 to 13 km/s). All of the simulations and experiments involved the same target configuration. Figure 6 indicates that the scaling of perforation size with normal impact momentum, applied by Christiansen and Friesen[9] to experimental data at velocities below 8 km/s, can be extrapolated to much of the velocity range of interest in orbital debris impact applications.

The simulations presented here were performed for projectile mass, impact obliquity, and impact velocity combinations, which perforate the target plate. However, some experimental data describe RCC damage under less severe impact conditions. Christiansen and Friesen[9] discuss light gas gun data for impact conditions, which result in only surface damage, partial penetration, delamination, and rear surface coating spall. They correlate the depth of penetration with a function of projectile density, target density, and normal impact velocity, and also indicate a threshold energy range for projectiles, which penetrate the upper-surface coating, spall the rear surface, and fully penetrate the target.

Accurate simulation of these experiments will require a high-resolution mesh and material models capable of describing rather complex damage mechanisms. It might call for additional mechanical properties testing, perhaps at elevated temperatures and high strain rates, to support the development and validation of very general strength models. Numerical methods and material models validated against partial penetration experiments can be applied to predict ballistic thresholds, for example, the impact velocity associated with a 50% probability of perforation for a given projectile mass and impact obliquity.

Conclusions

The present paper has formulated an anisotropic, rate-dependent material model for use in the simulation of hypervelocity impact problems. The material model was developed to study orbital debris impact effects on reinforced carbon–carbon materials and has been validated in simulations of hypervelocity impact experiments conducted at 7 km/s. The validated model was applied to simulate impacts at velocities beyond the experimental range. The simulation results indicate that momentum scaling, used to correlate a wide range of experiments below 8 km/s, can be applied to predict perforation diameters for reinforced carbon–carbon targets at velocities as high as 13 km/s. The ability of reinforced carbon–carbon to retain its strength at high temperatures suggests that accurate strength models of this material are important in simulations of impact effects over the entire orbital debris velocity range.

The use of composite materials in spacecraft applications complicates both experimental and computational studies of impact effects. High-cost materials with long fabrication lead times, such as reinforced carbon–carbon, and the limitations of current experimental impact techniques motivate the increased use of computer simulation in the design of spacecraft for micrometeoroid and orbital debris impact effects.

Acknowledgments

This work was supported by the Space Science Branch of NASA Johnson Space Center (NAG 9-1244) and by the National Science Foundation (CMS 99-12475). Computer time support was provided by the Texas Advanced Computing Center at the University of Texas at Austin and the Arctic Region Supercomputing Center at the University of Alaska Fairbanks.

References

[1] Windhorst, T., and Blount, G., "Carbon–Carbon Composites: A Summary of Recent Developments and Applications," *Materials and Design*, Vol. 18, No. 1, 1997, pp. 11–15.

[2] Schmidt, D. L., Davidson, K. E., and Theibert, L. S., "Unique Applications of Carbon–Carbon Composite Materials (Part One)," *SAMPE Journal*, Vol. 35, No. 1, 1999, pp. 27–39.

[3] Savage, G., *Carbon-Carbon Composites*, Chapman and Hall, London, 1993, p. 306.

[4] Ohlhorst, C. W., Vaughn, W. J., Ransone, P. O., and Tsou, H. T., "Thermal Conductivity Database of Various Structural Carbon–Carbon Composite Materials," NASA TM 1997-4787, Nov. 1997.

[5] *Report of the Columbia Accident Investigation Board*, Vol. 1, Government Printing Office, Washington, DC, Aug. 2003, Chap. 3.

[6] Lu, W.-Y., Antoun, B. R., Korellis, J. S., Scheffel, S., Lee, M. Y., Hardy, R. D., and Costin, L. S., "Material Characterization of Shuttle Thermal Protection System for Impact Analyses," AIAA Paper 2004-0945, Jan. 2004.

[7] Gwinn, K. W., and Metzinger, K. E., "Analysis of Foam Impact onto the Columbia Shuttle Wing Leading Edge Panels Using Pronto3D/SPH," AIAA Paper 2004-0942, Jan. 2004.

[8] Kerr, J. H., Grosch, D. J., and Christiansen, E. L., "Impact Testing of Large Foam Projectiles," AIAA Paper 2004-0939, Jan. 2004.

[9] Christiansen, E. L., and Friesen, L., "Penetration Equations for Thermal Protection Materials," *International Journal of Impact Engineering*, Vol. 20, Nos. 1–5, 1997, pp. 153–164.

[10] Fahrenthold, E. P., and Park, Y. K., "Simulation of Foam Impact Effects on the Space Shuttle Thermal Protection System," *Journal of Spacecraft and Rockets*, Vol. 42, No. 2, 2005, pp. 201–207.

[11] Shivarama, R., and Fahrenthold, E. P., "An Ellipsoidal Particle-Finite Element Method for Hypervelocity Impact Simulation," *International Journal for Numerical Methods in Engineering*, Vol. 59, No. 5, 2004, pp. 737–753.

[12] Park, Y. K., and Fahrenthold, E. P., "A Kernel-Free Particle-Finite Element Method for Hypervelocity Impact Simulation," *International Journal for Numerical Methods in Engineering*, Vol. 63, No. 5, 2005, pp. 737–759.

[13] McGlaun, J. M., Thompson, S. L., and Elrick, M. G., "CTH: A Three Dimensional Shock Wave Physics Code," *International Journal of Impact Engineering*, Vol. 10, Nos. 1–4, 1990, pp. 351–360.

[14] Malvern, L. E., *Introduction to the Mechanics of a Continuous Medium*, Prentice–Hall, Englewood Cliffs, NJ, 1969, Chap. 4.

[15] Aly-Hassan, M. S., Hatta, H., Wakayama, S., Watanabe, M., and Miyagawa, K., "Comparison of 2D and 3D Carbon/Carbon Composites with Respect to Damage and Fracture Resistance," *Carbon*, Vol. 41, No. 5, 2003, pp. 1069–1078.

[16] Anand, K., Gupta, V., and Dartford, D., "Failure Mechanisms of Laminated Carbon–Carbon Composites—II. Under Shear Loads," *Acta Metallurgica et Materialia*, Vol. 42, No. 3, 1994, pp. 797–809.

[17] Fitzer, E., and Manocha, L. M., *Carbon Reinforcements and Carbon/Carbon Composites*, Springer-Verlag, New York, 1998, p. 224.

[18] Abali, F., Pora, A., and Shivakumar, K., "Modified Short Beam Shear Test for Measurement of Interlaminar Sheear Strength of Composites," *Journal of Composite Materials*, Vol. 37, No. 5, 2003, pp. 453–464.

[19] Papakonstantinou, C. G., Balaguru, P., and Lyon, R. E., "Comparative Study of High Temperature Composites," *Composites: Part B*, Vol. 32, No. 8, 2001, pp. 637–649.

[20] Edgar, L. C., David, B., and Mattison, K. F., "The Interlaminar Tensile and Shear Behavior of a Unidirectional C-C Composite," *Journal of Nuclear Materials*, Vol. 230, No. 3, 1996, pp. 226–232.

[21] Buckley, J. D., and Edie, D. D., *Carbon–Carbon Materials and Composites*, Noyes Publications, Westwood, NJ, 1993, pp. 217–219.

[22] Steinberg, D. J., "Equation of State and Strength Properties of Selected Materials," Lawrence Livermore National Lab., UCRL-MA-106439, Livermore, CA, Feb. 1996.

[23] Dowding, K. J., Beck, J. V., and Blackwell, K. J., "Estimation of Directional-Dependent Thermal Properties in a Carbon-Carbon Composite," *International Journal of Heat Mass Transfer*, Vol. 39, No. 15, 1996, pp. 3157–3164.

[24] Christiansen, E. L., "Investigation of Hypervelocity Impact Damage to Space Station Truss Tubes," *International Journal of Impact Engineering*, Vol. 10, Nos. 1–4, 1990, pp. 125–133.

[25] Destefanis, R., and Faraud, M., "Testing of Advanced Materials for High Resistance Debris Shielding," *International Journal of Impact Engineering*, Vol. 20, Nos. 1–5, 1997, pp. 209–222.

[26] Yew, C. H., and Kendrick, R. B., "A Study of Damage in Composite Panels Produced by Hypervelocity Impact," *International Journal of Impact Engineering*, Vol. 5, Nos. 1–4, 1987, pp. 729–738.

[27] Palmieri, D., Destefanis, R., Faraud, M., and Lambert, M., "Penetration Effectiveness of Inhibited Shaped Charge Launcher Projectiles and Solid Spheres on Spacecraft Shields," *International Journal of Impact Engineering*, Vol. 29, Nos. 1–10, 2003, pp. 513–526.

[28] Silling, S. A., Taylor, P. A., Wise, J. L., and Furnish, M. D., "Micromechanical Modeling of Advanced Materials," Sandia National Labs., SAND94-0129, Albuquerque, NM, April 1994.

[29] Logan, R. W., "Incorporating Non-Quadratic and Crystallographic Yields Surfaces in Finite Element Codes," Los Alamos National Lab., LA-CP-88-186, Los Alamos, NM, 1988.

[30] Hayhurst, C. J., Livingstone, I. H. G., Clegg, R. A., Destefanis, R., and Faraud, M., "Ballistic Limit Evaluation of Advanced Shielding Using Numerical Simulations," *International Journal of Impact Engineering*, Vol. 26, Nos. 1–10, 2001, pp. 309–320.

[31] Anderson, C. E., Cox, P. A., Johnson, G. R., and Maudlin, P. J., "A Constitutive Formulation for Anisotropic Materials Suitable for Wave Propagation Computer Programs—II," *Computational Mechanics*, Vol. 15, No. 3, 1994, pp. 201–223.

[32] Hill, R., *The Mathematical Theory of Plasticity*, Oxford Univ. Press, Oxford, 1950, Chap. 12.

[33] Fahrenthold, E. P., and Horban, B. A., "Thermodynamics of Continuum Damage and Fragmentation Models for Hypervelocity Impact," *International Journal of Impact Engineering*, Vol. 20, Nos. 1–5, 1997, pp. 241–252.

[34] Fahrenthold, E. P., and Park, Y. K., "Simulation of Hypervelocity Impact on Aluminum-Nextel-Kevlar Orbital Debris Shields," *International Journal of Impact Engineering*, Vol. 29, Nos. 1–10, 2003, pp. 227–235.

[35] Silling, S. A., "CTH Reference Manual: Johnson-Holmquist Ceramic Model," Sandia National Labs., SAND92-0576, Albuquerque, NM, Sept. 1992.

[36] Lyon, S. P., and Johnson, J. D. (eds.), "SESAME: The Los Alamos National Laboratory Equation of State Database," Los Alamos National Lab., LA-UR-92-3407, Los Alamos, NM, 1992.

[37] Curry, D. M., Pham, V. T., Norman, I., and Chao, D. C., "Oxidation of Reinforced Carbon–Carbon Subjected to Hypervelocity Impact," NASA TP-2000-209760, March 2000.

[38] Lyons, L., Christiansen, E. L., and Kerr, J. H., "Hypervelocity Impact Testing of Reinforced Carbon–Carbon Composites," NASA Johnson Space Center, Rept. JSC 23898, May 1998.

S. Bouslog
Associate Editor